Materials Today Bio 11 (2021) 100120

Contents lists available at ScienceDirect

Materials Today Bio

journal homepage: www.journals.elsevier.com/materials-today-bio

Long-term stabilized amorphous calcium carbonate—an ink for bio-inspired 3D printing

H. Shaked, I. Polishchuk, A. Nagel, Y. Bekenstein, B. Pokroy *

Department of Materials Science and Engineering and the Russell Berrie Nanotechnology Institute, Technion – Israel Institute of Technology, Haifa, 32000, Israel

ARTICLE INFO

Keywords:
ACC
Stabilization
Bioinspired
Ceramics
Robocasting
Calcite

ABSTRACT

Biominerals formed by organisms in the course of biomineralization often demonstrate complex morphologies despite their single-crystalline nature. This is achieved owing to the crystallization via a predeposited amorphous calcium carbonate (ACC) phase, a precursor that is particularly widespread in biominerals. Inspired by this natural strategy, we used robocasting, an additive manufacturing three-dimensional (3D) printing technique, for printing 3D objects from novel long-term, Mg-stabilized ACC pastes with high solids loading. We demonstrated, for the first time, that the ACC remains stable for at least a couple of months, even after printing. Crystallization, if desired, occurs only after the 3D object is already formed and at temperatures significantly lower than those of common postprinting sintering. We also examined the effects different organic binders have on the crystallization, the morphology, and the final amount of incorporated Mg. This novel bio-inspired method may pave the way for a new bio-inspired route to low-temperature 3D printing of ceramic materials for a multitude of applications.

1. Introduction

Calcium carbonate ($CaCO_3$) is the biomineral most abundantly used by various organisms to form skeletons, protective shells [1], teeth [2], and optical lenses [3]. While the commonest thermodynamically stable polymorphs of biogenic $CaCO_3$ are calcite and aragonite, the metastable polymorph amorphous calcium carbonate (ACC) has gained increasing interest owing to its widespread function as a precursor to crystalline $CaCO_3$. As a precursor, ACC leads to the formation of crystals exhibiting unique morphologies and enhanced physical properties [2–9]. Amorphous-to-crystalline transformation is known to facilitate the incorporation of organic and inorganic additives [10–13]. Mg is a common impurity in biogenic $CaCO_3$, and in biogenic calcite, it can reach up to 40 at. % [14,15], a value substantially higher than its thermodynamic solubility limit (~2 at. %) [16]. Incorporation of Mg is known to stabilize ACC, as well as to tune the hardness and change the morphology of the formed crystals; in addition, it induces lattice distortions [17–20]. The ability to mimic the formation of intricately shaped crystals incorporating high amounts of various chemical species would be of great interest to materials scientists. The stability of intracrystalline organic additives is poor at elevated temperatures [12,13]. Our approach does not require processing at elevated temperatures, thereby enabling the preservation of both the intricate shapes and the presence of even organic additives in the final crystalline lattice. Here, for the first time, we demonstrate long-term stabilization of ACC under ambient conditions, thereafter, used to form an easily handled amorphous ink, and utilize it to form three-dimensional (3D) models via an emerging technique of 3D printing. Bio-inspired 3D printing of ACC models may shed more light on the advantages of this phase from a materials point of view and deepen our understanding of the non-classical crystallization route commonly found in nature.

3D printing is a revolutionary manufacturing technique already used in various fields [21–25]. Given the growing demand for ceramic materials, several 3D printing methods have been developed for the fabrication of ceramic products [26]. Powder-based printing exploits the ability of a powder to bond in different media by using either laser sintering [27,28] or chemical binders [29,30]. Solid–based techniques use solidified laser-cut thin sheets of ceramics as per computed design, later layered and laminated together [31] or by using ceramic powders bonded to thermoplastic polymers to form a flexible composite filament [32]. Liquid-based techniques use photoreactive polymeric resins with embedded ceramic powders [33,34]. Robocasting is an additive manufacturing technique that is applicable in a wide variety of ceramic materials. Using this technique, a preprepared semiliquid paste with high ceramic loading is extruded through a thin nozzle [35,36]. The paste is required to provide an appropriate viscosity under stress,

* Corresponding author.
E-mail address: bpokroy@technion.ac.il (B. Pokroy).

https://doi.org/10.1016/j.mtbio.2021.100120
Received 27 April 2021; Received in revised form 27 May 2021; Accepted 30 May 2021
Available online 19 June 2021

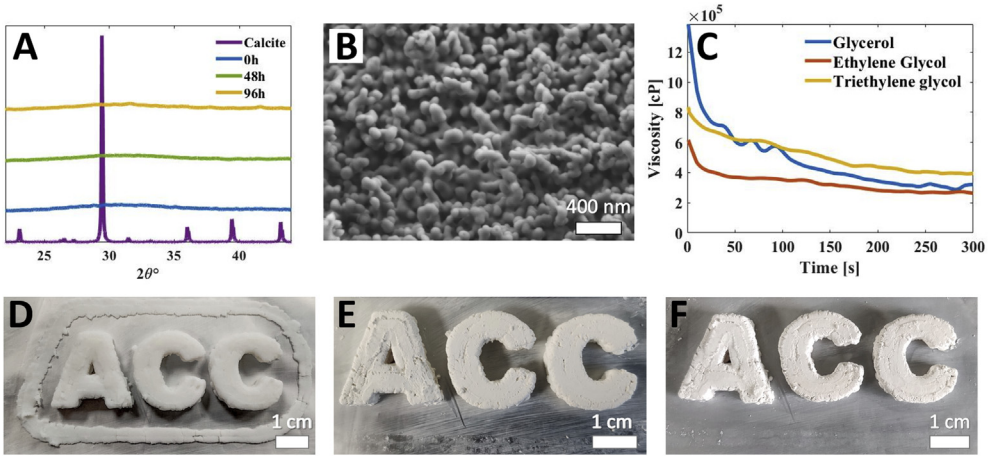

Fig. 1. (A) XRD patterns collected at a wavelength of Cu K-α 1.5406 Å from 'as synthesized' (0 h) powdered ACC after its storage in acetone excess for 48 and 96 h. Diffraction patterns are compared with those of crystalline calcite. (B) HR-SEM image demonstrating the morphology of obtained ACC. (C) Viscosity of prepared 50/50 pastes as a function of time for a constant shear rate. The decrease in viscosity over time until a plateau is reached is consistent with non-Newtonian shear-thinning materials [50,51]. (D–F) 50/50 ACC printed models from EG paste forming the word 'ACC', (D) immediately after printing, (E) after low-temperature sintering, and (F) after crystallization treatment in an autoclave, sample height, 6 mm.

allowing self-support and extrudability, and it should contain only a few, if any, agglomerates and a binder which, if required, can be easily removed after use [37]. The standard ceramic robocasting procedure forms a green body, a weakly bound mixture of a powder and an organic or inorganic additive, that usually requires high-temperature sintering. However, in our case, we eliminate the need in postprinting sintering and enable low-temperature hardening of the printed material instead. Overcoming this limitation will enable incorporation and preservation of various organic additives in a composite functional material which can be further used in a variety of applications such as cultural heritage reconstruction, artificial reef formation, and bio-medical engineering (e.g. drug delivery).

Studies have revealed the potential inherent in bio-inspired 3D printing. Formation of highly porous ceramics inspired by wood and bones [38,39], formation of hierarchical crack-controlled materials resembling nacre and spider silk [40,41], and formation of superhydrophobic materials inspired by the lotus flower [42] are just a few examples. Bio-inspired 3D printing of crystalline calcium salts has focused mainly on calcium phosphates because of their abundance in natural organisms and their compatibility with bone-implant applications [43–45]. Currently, usage of $CaCO_3$ in 3D printing is mainly limited to crystalline powders bonded with aqueous binders [46,47]. Up to now, 3D printing of ACC has been contraindicated by its heat intolerance as well as by its inability to stabilize for long periods of time.

Here, by using the robocasting method, we present an innovative route to the bio-inspired 3D printing of high-Mg ACC. We also introduce a novel storage protocol that allows maintaining the amorphous nature of ACC powder for at least several days. In contrast to current technologies, our approach involves sintering at low temperatures (relatively to classic sintering) and on-demand crystallization. We also examined the influence exerted by different organic binders on the crystalline structure and the morphology of the printed models.

2. Materials and methods

2.1. Powder preparation

Aqueous solutions of $CaCl_2 \cdot 2H_2O$ (73.5 g, 0.5 L), $MgCl_2 \cdot 6H_2O$ (101.655 g, 0.5 L), and Na_2CO_3 (52.995 g, 0.5 L) at 1 M concentration were prepared and stored overnight at 8 °C. A total of 50/50, 60/40, and 70/30 ratios of Ca:Mg solutions were mixed in a glass beaker for 5 min. An equivalent amount of Na_2CO_3 solution was added to the beaker with active mixing, preserving a 1:1 ion ratio between CO_3^{-2} and (Ca^{+2}+Mg^{+2}). The suspension was rapidly filtered through a Buchner funnel with grade 5 Whatman filter paper, followed by washing with water and acetone. After remaining under suction for 10 min, the filtered powder was dried for 3 h in a vacuum oven at 25 °C, 0.1 MPa. Storage of the dried ACC powder was maintained by its submergence in an excess of acetone.

2.2. Paste preparation

Stored powder was dried, grounded with a mortar and pestle, and then mixed with a dispersant (comprising commercial corn oil [48] at a fixed ratio of 0.1 ml per 1 g of powder) and varying amounts of three different binders, ethylene glycol (EG) (99.8%, AR, Merck), triethylene glycol (TEG) (≥99%, Merck), and glycerol (GLY) (anhydrous, 99.5%, AR, Bio-Lab Ltd.). The powder was slowly added to the binder and was hand mixed until a solid firm paste was obtained. Solids loading of the mixed paste was kept between 55 and 65%, i.e. 1 g of powder for 0.5–0.8 ml of dispersant-binder mixture.

2.3. 3D printing and after treatment

3D models were printed using the commercially available Hyrel 3D Engine-SR printer with a KR2-15 stainless steel extrusion head with a 1-mm nozzle. 3D computer-aided design (3D-CAD) of the printed models was sketched using Fusion 360 (Autodesk). The 3D-CAD was converted to an STL file, which was uploaded to the printer, where it was sliced, and the G-code was written. The printed models were placed in a vacuum oven for low-temperature sintering overnight at 150 °C, 0.1 MPa. The dry models were then transferred to the autoclave for the final crystallization step under humid conditions for 1 h at 100 °C, 0.1 MPa, with relative humidity (RH) of 97%, where the remaining 3% are of moisture. Later, the models were dried in a vacuum oven for 3 h at 75 °C, 0.1 MPa.

2.4. High-resolution scanning electron microscopy

Samples were imaged using the Zeiss Ultra-Plus FEG-SEM at 1–2 keV with 4–4.2 mm working distance. Energy-dispersive spectroscopy (EDS) was performed after carbon coating at 7 kV.

2.5. X-ray diffraction

Diffraction patterns of powdered samples were acquired using the Rigaku SmartLab 9 kW high-resolution diffraction system at a wavelength of Cu K-α 1.5406 Å and the Rigaku MiniFlex benchtop powder X-ray diffraction (XRD) instrument at a wavelength of Cu K-α 1.5406 Å.

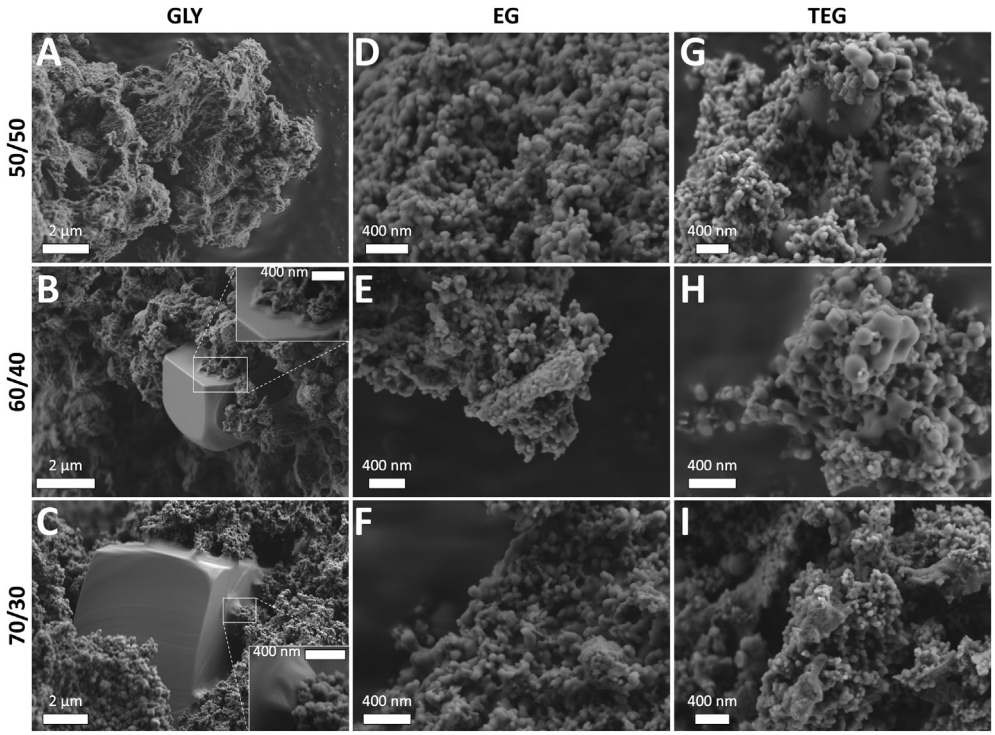

Fig. 2. HR-SEM images of the 3D-printed models after sintering. (A–C), with GLY binder; (D–F), with EG binder; (G–I), with TEG binder. Insets in (B) and (C) show magnified images of the 'feeding-stock' phenomenon.

2.6. Optical microscopy

Samples were imaged using the Olympus BX51 optical microscope with reflected light at x5-x20 magnifications.

2.7. Confocal microscopy

Sample roughness was measured using the Leica DCM 3D confocal microscope at x5 magnification.

2.8. Rheology

Viscosity of the pastes was examined using the HR-2 Discovery Hybrid Rheometer, in rotational mode. Rheological measurements were performed at room temperature (25 °C) at constant shear of 10 s^{-1} with at least 3 replicates performed for each test. Approximately 1 cm^3 of paste was used in each experiment in a plate–plate geometry with 8-mm diameter. The gap between the plates was set to 1.3 mm.

3. Results and discussion

3.1. Preparation of printable, Mg stabilized ACC paste and its viscosity

ACC was precipitated from solution in the presence of Mg. Different Ca:Mg ratios were tested, preserving a 1:1 ion ratio between CO_3^{-2} and (Ca^{+2}+Mg^{+2}). Each sample was labeled as per the Ca:Mg ratio used in the mixture, where 50/50 means 50% Ca solution and 50% Mg solution (e.g. 50 ml $CaCl_2$, 50 ml $MgCl_2$, and 100 ml $NaCO_3$ comprise 200 ml of sample solution), the 60/40 and 70/30 solutions were labeled accordingly. Mixing of the solutions resulted in the immediate precipitation of ACC. High amounts of ACC were synthesized from 1 M stock solutions, resulting in a yield of ~92%. To accumulate the amount of powder needed for 3D printing, an appropriate storage method was needed. We found that ACC powders, when stored in an excess of acetone, remain amorphous for long periods of time. This storage protocol enabled obtaining up to 40 gr of stabilized ACC in one experimental batch. As evidenced by XRD patterns, the amorphous nature of ACC powder was preserved for 90–120 h after synthesis (Fig. 1A) by its storage in an excess of acetone. Morphology of the synthesized ACC is depicted in Fig. 1B. To prepare a printable paste, ACC powder was individually mixed with a dispersant (corn oil) and one of the three different binders—GLY, EG, and TEG. The dispersant and the binders present a non-toxic, non-volatile behavior at room temperature (RT), allowing the facile formation of paste and a green printing process. All selected materials are non-hydrous, allowing the conservation of the amorphous nature. Viscosities of the 50/50 resultant pastes were measured. Viscosity, among other parameters, is crucial in a printable paste that must be extrudable, non-phase–separating, durable, and easily handled. The pastes prepared as described previously undergo changes in viscosity over time. For a constant shear rate, a non-Newtonian shear-thinning behavior was observed here, with viscosities ranging from 264,000 to 394,000 [cP], consistent with ceramic pastes with high solids loading [49–51]. No phase separation was observed in our pastes (Fig. 1C). Solids loading (i.e. the amount of suspended solids in a paste) has been shown to influence the final density of sintered ceramics [52]. High solids loadings are known to have a central role in the mechanical properties of the final product, resulting in a firmer and more stress-resilient ceramic part [53,54]. High solids-loading pastes (>65%) were difficult to measure as they cracked when applied with initial shear force and were not easy to handle. Lower solids-loading pastes (<55%) could not be extruded without forcing phase separation. These findings led us to choose solids loadings of 55–65% to prevent undesirable results.

3.2. 3D printing

3D printing of the prepared pastes was performed on aluminum foil. Folded aluminum foil was fixated to the printer's print bed for fast and easy transfer to the succeeding steps. The printing resolution was limited by the nozzle head used, which allowed accuracy within 1 mm. Initially, two 'skirts' were printed around each model to allow priming of the extruder, thereby ensuring smooth and stable flow. The ACC models were then printed and transferred to a vacuum oven for

overnight sintering (150 °C, 0.1 MPa, 15 h), followed by exposure to humid conditions in an autoclave (100 °C, 0.1 MPa, 1 h, 97% RH) for final crystallization. Humidity-induced crystallization is caused by surface adsorption of water molecules, which results in partial dissolution and reprecipitation of the $CaCO_3$ into a more stable, crystalline formation [55]. After such treatment, printed models exhibited shape retention without dimensional distortions or significant structural cracks or fractures and allowed the removal of the binder by means of low-temperature sintering (Fig. 1D–F). Higher magnification images of the autoclave-treated models and representative images for the printing accuracy as well as surface roughness measurements showing a lateral roughness of 35.4 μm can be seen in Fig. S1. Owing to the limited thermal stability of ACC and its susceptibility to spinodal decomposition [12,13], sintering was carried out at a maximum temperature of 150 °C. This significant decrease in sintering temperatures is essential for energy conservation purposes.

3.3. Morphology and composition

Changes in morphology, depending on the binder used, were observed. In EG- and TEG-printed models, the spherical morphology of ACC was preserved after the sintering step (Fig. 2D–I). TEG models (Fig. 2G–I) present larger spheres that are a result of ACC coarsening. On the other hand, the crystalline morphologies of GLY 60/40 and 70/30 models revealed clear rhombohedral facets (Fig. 2B–C), implying that for GLY models, crystallization had probably occurred during the sintering step. We believe that a 'feeding-stock' phenomenon takes place, leading to the possibility of slow-paced crystallization in which the ACC particles are used as a $CaCO_3$ reservoir, as observed in biomineralization in nature (Fig. 2B, C insets) [56,57]. After autoclave treatment, the morphology changed drastically, and crystalline morphology can be seen in all models (Fig. S2).

Chemical compositions of the sintered ACC models and their respective Ca:Mg ratios were analyzed by means of EDS (Fig. S3). As expected, the 50/50 ACC models exhibited higher levels of Mg incorporation than those of 60/40 or 70/30 models. The highest level of incorporated Mg, with ~36 at. %, was observed in the case of the 50/50 GLY model, the higher the Mg content, the more significant the difference in incorporation levels between GLY and the other binders. We assume that stabilization of ACC obtained with TEG and EG binders may result in faster diffusion routes for Mg ions, while the GLY binder boosts crystallization, altogether leading to more complicated diffusion routes which result in higher levels of Mg incorporation.

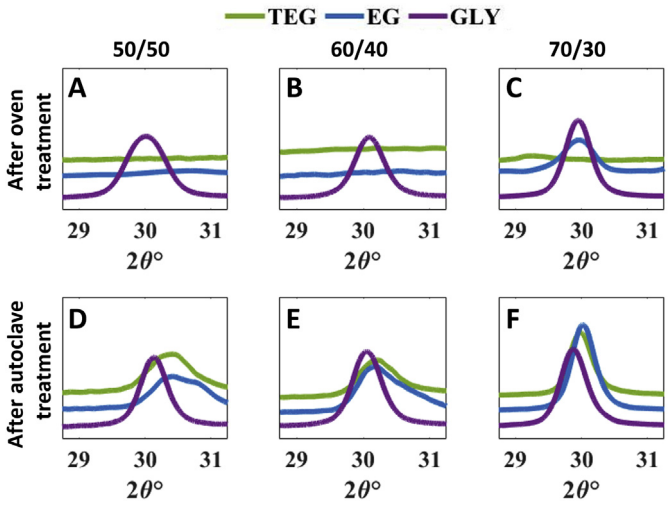

Fig. 3. The (104) diffraction peak of calcite (XRD patterns collected at a wavelength of Cu K-α 1.5406 Å). (A–C), after oven treatment; (B–F), after autoclave treatment.

3.4. Crystallization of the ACC models

The relationship between the binder and the crystallization process was examined in both the oven sintering and the autoclave crystallization postprinting steps. After oven sintering, both the EG- and the TEG-stabilized ACC models preserved their amorphous nature, showing a very mild degree of crystallization. Preservation of ACC for long periods of time was proven possible either by unique synthesis routes resulting in minimal amounts of the product or by conservation in unique conditions [58–61]; herein, we present ACC stabilization when preserved at ambient conditions for several months. The 70/30 models showed susceptibility to crystallization owing to their reduced stability associated with their lower levels of Mg incorporation (Fig. 3A–C). The smallest amount of crystallization after oven sintering was that of calcite with its clear (006) preferred orientation, as well as of some aragonite revealing the (221) and (123) diffraction peaks (Fig. S4). We believe that the (006) preferred orientation results from the organic environment of the printed models. On the other hand, the GLY-stabilized ACC model demonstrated complete crystallization after oven sintering, which can be attributed to its highly hygroscopic nature [62]. The high-humidity environment within the autoclave facilitated rapid crystallization of all models, resulting in the formation of both calcite and aragonite phases (Fig. 3D–F). Further evidence of Mg incorporation into the structure of the printed models during the amorphous-to-crystalline transformation is provided by the shift in the (104) diffraction peak position to higher 2θ angles (Mg is a smaller ion than Ca) [63].

Profile fitting [64] of the (104) single-diffraction peak revealed a relationship between the binder and the crystallite size in printed models (Fig. S5). GLY was able to promote the formation of larger crystals than those formed with EG; the smallest crystals were observed when TEG was used as the binder. This trend was observed for all samples with varying Ca:Mg ratios, confirming a clear dependency between the grain size and the binder. GLY was the only binder that promoted slow crystallization during the oven treatment, whereas in the presence of either EG or TEG, crystallization was rapidly induced by the humid environment within the autoclave. Therefore, slower growth rates led to the formation of larger crystals, whereas rapid crystallization promoted the formation of smaller crystals.

4. Conclusions

This study presents a novel bio-inspired approach to the printing of 3D complex structures using robocasting of printable, long-term stabilized ACC pastes with high solids loading (55–65%). Stabilization of ACC was achieved by the incorporation of foreign atoms such as Mg as well as by the storage environment. The amorphous nature of the obtained printable ACC pastes was retained for up to some months, even after low-temperature sintering at 150 °C. The post-sintered printed ACC 3D models exhibited no shrinkage and maintained their initial dimensions and complex shapes. We further showed that the choice of the binder affected the amount of incorporated Mg, as well as the stabilization and the final morphology of the ACC models. EG and TEG preserved the amorphous nature of the ACC models for up to several months after printing, whereas GLY boosted their crystallization possibly due to its highly hygroscopic nature. GLY also facilitated the formation of larger crystals with higher Mg incorporation. In addition, GLY presented a 'feeding-stock' morphology resembling that of ACC during its transformation to a crystalline phase in nature, thereby serving as a $CaCO_3$ reservoir enabling the formation of large crystals with unique morphologies and enhanced characteristics. This novel approach to 3D printing of ACC may highlight the advantages of this phase as a precursor to crystalline $CaCO_3$ and open new routes to energy-efficient 3D printing of ceramics for multiple applications.

Contributions

Hadar Shaked: Performed the experiments wrote paper and methodology. Iryna Polishchuk: Conceptualization and paper writing Alina Nagel: Helped with part of the experiments. Yehonadav Bekenstein: Paper editing and Methodology. Boaz Pokroy: Conceptualization, Supervision, Methodology and Paper writing.

Declaration of competing interest

The authors declare that they have no known competing financial interests or personal relationships that could have appeared to influence the work reported in this paper.

Acknowledgments

This research was partly funded by the European Research Council under the European Union's Seventh Framework Program (FP/2013–2018)/ERC Grant agreement no. 336077.

The authors thank Prof. Shlomo Magdassi (The Hebrew University of Jerusalem) for the helpful discussion.

Appendix A. Supplementary data

Supplementary data to this article can be found online at https://doi.org/10.1016/j.mtbio.2021.100120.

References

[1] J. Aizenberg, S. Weiner, L. Addadi, Coexistence of amorphous and crystalline calcium carbonate in skeletal tissues, Connect. Tissue Res. 44 (2003) 20–25, https://doi.org/10.1080/03008200390152034.

[2] E. Beniash, J. Aizenberg, L. Addadi, S. Weiner, Amorphous calcium carbonate transforms into calcite during sea urchin larval spicule growth, Proc. R. Soc. Lond. Ser. B Biol. Sci. 264 (1997) 461–465, https://doi.org/10.1098/rspb.1997.0066.

[3] J. Aizenberg, A. Tkachenko, S. Weiner, L. Addadi, G. Hendler, Calcitic microlenses as part of the photoreceptor system in brittlestars, Nature 412 (2001) 819–822, https://doi.org/10.1038/35090573.

[4] S. Weiner, L. Addadi, Crystallization pathways in biomineralization, Annu. Rev. Mater. Res. 41 (2011) 21–40, https://doi.org/10.1146/annurev-matsci-062910-095803.

[5] L. Addadi, S. Raz, S. Weiner, Taking advantage of disorder: amorphous calcium carbonate and its roles in biomineralization, Adv. Mater. 15 (2003) 959–970, https://doi.org/10.1002/adma.200300381.

[6] A.-W. Xu, Y. Ma, H. Cölfen, Biomimetic mineralization, J. Mater. Chem. 17 (2007) 415–449, https://doi.org/10.1039/B611918M.

[7] M.J. Olszta, D.J. Odom, E.P. Douglas, L.B. Gower, A new paradigm for biomineral formation: mineralization via an amorphous liquid-phase precursor, Connect. Tissue Res. 44 (2003) 326–334, https://doi.org/10.1080/03008200390181852.

[8] N. Nassif, N. Pinna, N. Gehrke, M. Antonietti, C. Jager, H. Colfen, Amorphous layer around aragonite platelets in nacre, Proc. Natl. Acad. Sci. Unit. States Am. 102 (2005) 12653–12655, https://doi.org/10.1073/pnas.0502577102.

[9] L.B. Gower, D.J. Odom, Deposition of calcium carbonate films by a polymer-induced liquid-precursor (PILP) process, J. Cryst. Growth 210 (2000) 719–734, https://doi.org/10.1016/S0022-0248(99)00749-6.

[10] S. Borukhin, L. Bloch, T. Radlauer, A.H. Hill, A.N. Fitch, B. Pokroy, Screening the incorporation of amino acids into an inorganic crystalline host: the case of calcite, Adv. Funct. Mater. 22 (2012) 4216–4224, https://doi.org/10.1002/adfm.201201079.

[11] Y.-Y. Kim, J.D. Carloni, B. Demarchi, D. Sparks, D.G. Reid, M.E. Kunitake, C.C. Tang, M.J. Duer, C.L. Freeman, B. Pokroy, K. Penkman, J.H. Harding, L.A. Estroff, S.P. Baker, F.C. Meldrum, Tuning hardness in calcite by incorporation of amino acids, Nat. Mater. 15 (2016) 903–910, https://doi.org/10.1038/nmat4631.

[12] I. Polishchuk, A.A. Bracha, L. Bloch, D. Levy, S. Kozachkevich, Y. Etinger-Geller, Y. Kauffmann, M. Burghammer, C. Giacobbe, J. Villanova, G. Hendler, C.Y. Sun, A.J. Giuffre, M.A. Marcus, L. Kundanati, P. Zaslansky, N.M. Pugno, P.U.P.A. Gilbert, A. Katsman, B. Pokroy, Coherently aligned nanoparticles within a biogenic single crystal: a biological prestressing strategy, Science 358 (2017) 1294–1298, https://doi.org/10.1126/science.aaj2156.

[13] E. Seknazi, S. Kozachkevich, I. Polishchuk, N. Bianco Stein, J. Villanova, J.P. Suuronen, C. Dejoie, P. Zaslansky, A. Katsman, B. Pokroy, From spinodal decomposition to alternating layered structure within single crystals of biogenic magnesium calcite, Nat. Commun. 10 (2019) 1–9, https://doi.org/10.1038/s41467-019-12168-8.

[14] S. Raz, S. Weiner, L. Addadi, formation of high-magnesian calcites via an amorphous precursor phase: possible biological implications, Adv. Mater. 12 (2000) 38–42, https://doi.org/10.1002/(SICI)1521-4095(200001)12:1<38::AID-ADMA38>3.0.CO;2-I.

[15] G. Falini, M. Gazzano, A. Ripamonti, Crystallization of calcium carbonate in presence of magnesium and polyelectrolytes, J. Cryst. Growth 137 (1994) 577–584, https://doi.org/10.1016/0022-0248(94)91001-4.

[16] Y. Politi, D.R. Batchelor, P. Zaslansky, B.F. Chmelka, J.C. Weaver, I. Sagi, S. Weiner, L. Addadi, Role of magnesium ion in the stabilization of biogenic amorphous calcium carbonate: a Structure−Function investigation, Chem. Mater. 22 (2010) 161–166, https://doi.org/10.1021/cm902674h.

[17] Y. Ma, S.R. Cohen, L. Addadi, S. Weiner, Sea urchin tooth design: an "all-calcite" polycrystalline reinforced fiber composite for grinding rocks, Adv. Mater. 20 (2008) 1555–1559, https://doi.org/10.1002/adma.200702842.

[18] J.D. Rodriguez-Blanco, S. Shaw, P. Bots, T. Roncal-Herrero, L.G. Benning, The role of pH and Mg on the stability and crystallization of amorphous calcium carbonate, J. Alloys Compd. 536 (2012) S477–S479, https://doi.org/10.1016/j.jallcom.2011.11.057.

[19] E. Loste, R.M. Wilson, R. Seshadri, F.C. Meldrum, The role of magnesium in stabilising amorphous calcium carbonate and controlling calcite morphologies, J. Cryst. Growth 254 (2003) 206–218, https://doi.org/10.1016/S0022-0248(03)01153-9.

[20] E. Seknazi, B. Pokroy, Residual strain and stress in biocrystals, Adv. Mater. 30 (2018) 1–6, https://doi.org/10.1002/adma.201707263.

[21] B.G. Compton, J.A. Lewis, 3D-Printing of lightweight cellular composites, Adv. Mater. 26 (2014) 5930–5935, https://doi.org/10.1002/adma.201401804.

[22] K. Sun, T.-S. Wei, B.Y. Ahn, J.Y. Seo, S.J. Dillon, J.A. Lewis, 3D printing of interdigitated Li-ion microbattery architectures, Adv. Mater. 25 (2013) 4539–4543, https://doi.org/10.1002/adma.201301036.

[23] D.B. Kolesky, R.L. Truby, A.S. Gladman, T.A. Busbee, K.A. Homan, J.A. Lewis, 3D bioprinting of vascularized, heterogeneous cell-laden tissue constructs, Adv. Mater. 26 (2014) 3124–3130, https://doi.org/10.1002/adma.201305506.

[24] A. Kamyshny, S. Magdassi, Conductive nanomaterials for printed electronics, Small 10 (2014) 3515–3535, https://doi.org/10.1002/smll.201303000.

[25] N. Zhou, Y. Bekenstein, C.N. Eisler, D. Zhang, A.M. Schwartzberg, P. Yang, A.P. Alivisatos, J.A. Lewis, Perovskite nanowire–block copolymer composites with digitally programmable polarization anisotropy, Sci. Adv. 5 (2019), https://doi.org/10.1126/sciadv.aav8141 eaav8141.

[26] Z. Chen, Z. Li, J. Li, C. Liu, C. Lao, Y. Fu, C. Liu, Y. Li, P. Wang, Y. He, 3D printing of ceramics: a review, J. Eur. Ceram. Soc. 39 (2019) 661–687, https://doi.org/10.1016/j.jeurceramsoc.2018.11.013.

[27] P. Bertrand, F. Bayle, C. Combe, P. Goeuriot, I. Smurov, Ceramic components manufacturing by selective laser sintering, Appl. Surf. Sci. 254 (2007) 989–992, https://doi.org/10.1016/j.apsusc.2007.08.085.

[28] J. Deckers, S. Meyers, J.P. Kruth, J. Vleugels, Direct selective laser sintering/melting of high density alumina powder layers at elevated temperatures, Phys. Procedia 56 (2014) 117–124, https://doi.org/10.1016/j.phpro.2014.08.154.

[29] J. Will, R. Melcher, C. Treul, N. Travitzky, U. Kneser, E. Polykandriotis, R. Horch, P. Greil, Porous ceramic bone scaffolds for vascularized bone tissue regeneration, J. Mater. Sci. Mater. Med. 19 (2008) 2781–2790, https://doi.org/10.1007/s10856-007-3346-5.

[30] D. Ke, S. Bose, Effects of pore distribution and chemistry on physical, mechanical, and biological properties of tricalcium phosphate scaffolds by binder-jet 3D printing, Addit. Manuf. 22 (2018) 111–117, https://doi.org/10.1016/j.addma.2018.04.020.

[31] B. Dermeik, N. Travitzky, Laminated object manufacturing of ceramic-based materials, Adv. Eng. Mater. 22 (2020) 2000256, https://doi.org/10.1002/adem.202000256.

[32] C. Esposito Corcione, F. Gervaso, F. Scalera, S.K. Padmanabhan, M. Madaghiele, F. Montagna, A. Sannino, A. Licciulli, A. Maffezzoli, Highly loaded hydroxyapatite microsphere/PLA porous scaffolds obtained by fused deposition modelling, Ceram. Int. 45 (2019) 2803–2810, https://doi.org/10.1016/j.ceramint.2018.07.297.

[33] E. Shukrun Farrell, Y. Schilt, M.Y. Moshkovitz, Y. Levi-Kalisman, U. Raviv, S. Magdassi, 3D printing of ordered mesoporous silica complex structures, Nano Lett. 20 (2020) 6598–6605, https://doi.org/10.1021/acs.nanolett.0c02364.

[34] I. Cooperstein, S.R.K.C. Indukuri, A. Bouketov, U. Levy, S. Magdassi, 3D printing of micrometer-sized transparent ceramics with on-demand optical-gain properties, Adv. Mater. 32 (2020) 2001675, https://doi.org/10.1002/adma.202001675.

[35] E. Peng, D. Zhang, J. Ding, Ceramic robocasting: recent achievements, potential, and future developments, Adv. Mater. 30 (2018) 1802404, https://doi.org/10.1002/adma.201802404.

[36] A. Zocca, P. Colombo, C.M. Gomes, J. Günster, Additive manufacturing of ceramics: issues, potentialities, and opportunities, J. Am. Ceram. Soc. 98 (2015) 1983–2001, https://doi.org/10.1111/jace.13700.

[37] N. Travitzky, A. Bonet, B. Dermeik, T. Fey, I. Filbert-Demut, L. Schlier, T. Schlordt, P. Greil, Additive manufacturing of ceramic-based materials, Adv. Eng. Mater. 16 (2014) 729–754, https://doi.org/10.1002/adem.201400097.

[38] C. Minas, D. Carnelli, E. Tervoort, A.R. Studart, 3D printing of emulsions and foams into hierarchical porous ceramics, Adv. Mater. 28 (2016) 9993–9999, https://doi.org/10.1002/adma.201603390.

[39] L. Alison, S. Menasce, F. Bouville, E. Tervoort, I. Mattich, A. Ofner, A.R. Studart, 3D printing of sacrificial templates into hierarchical porous materials, Sci. Rep. 9 (2019) 409, https://doi.org/10.1038/s41598-018-36789-z.

[40] G.X. Gu, I. Su, S. Sharma, J.L. Voros, Z. Qin, M.J. Buehler, Three-dimensional-printing of bio-inspired composites, J. Biomech. Eng. 138 (2016) 1–16, https://doi.org/10.1115/1.4032423.

[41] R. Mirzaeifar, L.S. Dimas, Z. Qin, M.J. Buehler, Defect-tolerant bioinspired hierarchical composites: simulation and experiment, ACS Biomater. Sci. Eng. 1 (2015) 295–304, https://doi.org/10.1021/ab500120f.
[42] R. Xing, R. Huang, W. Qi, R. Su, Z. He, Three-dimensionally printed bioinspired superhydrophobic PLA membrane for oil-water separation, AIChE J. 64 (2018) 3700–3708, https://doi.org/10.1002/aic.16347.
[43] C. Bergmann, M. Lindner, W. Zhang, K. Koczur, A. Kirsten, R. Telle, H. Fischer, 3D printing of bone substitute implants using calcium phosphate and bioactive glasses, J. Eur. Ceram. Soc. 30 (2010) 2563–2567, https://doi.org/10.1016/j.jeurceramsoc.2010.04.037.
[44] P. Miranda, E. Saiz, K. Gryn, A.P. Tomsia, Sintering and robocasting of β-tricalcium phosphate scaffolds for orthopaedic applications, Acta Biomater. 2 (2006) 457–466, https://doi.org/10.1016/j.actbio.2006.02.004.
[45] R. Trombetta, J.A. Inzana, E.M. Schwarz, S.L. Kates, H.A. Awad, 3D printing of calcium phosphate ceramics for bone tissue engineering and drug delivery, Ann. Biomed. Eng. 45 (2017) 23–44, https://doi.org/10.1007/s10439-016-1678-3.
[46] D. Mohan, N.F. Khairullah, Y.P. How, M.S. Sajab, H. Kaco, 3D printed laminated CaCO3-nanocellulose films as controlled-release 5-fluorouracil, Polymers 12 (2020) 986, https://doi.org/10.3390/polym12040986.
[47] M.C. Leu, B.K. Deuser, R.G. Landers, G.E. Hilmas, J.L. Watts, Freeze-form extrusion fabrication of functionally graded materials, CIRP Ann. - Manuf. Technol. (2012) 61, https://doi.org/10.1016/j.cirp.2012.03.050.
[48] D.J. Shaneield, Organic Additives and Ceramic Processing, with Applications in Powder Metallurgy, Ink and Paint, 1995.
[49] A. Zima, J. Czechowska, D. Siek, A. Ślósarczyk, Influence of magnesium and silver ions on rheological properties of hydroxyapatite/chitosan/calcium sulphate based bone cements, Ceram. Int. 43 (2017) 16196–16203, https://doi.org/10.1016/j.ceramint.2017.08.197.
[50] Y. Ryabenkova, A. Pinnock, P.A. Quadros, R.L. Goodchild, G. Möbus, A. Crawford, P.V. Hatton, C.A. Miller, The relationship between particle morphology and rheological properties in injectable nano-hydroxyapatite bone graft substitutes, Mater. Sci. Eng. C 75 (2017) 1083–1090, https://doi.org/10.1016/j.msec.2017.02.170.
[51] Abhijit P. Deshpande, J.M.K. Kumar, P.B. Sunil, Rheology of Complex Fluids, Springer New York, New York, NY, 2010, https://doi.org/10.1007/978-1-4419-6494-6.
[52] J.M.F. Ferreira, H.M.M. Diz, Effect of solids loading on slip-casting performance of silicon carbide slurries, J. Am. Ceram. Soc. 82 (1999) 1993–2000, https://doi.org/10.1111/j.1151-2916.1999.tb02031.x.
[53] J. Wei, J. Li, X. Song, Y. Feng, T. Qiu, Effects of solid loading on the rheological behaviors and mechanical properties of injection-molded alumina ceramics, J. Alloys Compd. 768 (2018) 503–509, https://doi.org/10.1016/j.jallcom.2018.07.036.
[54] T. Chen, A. Sun, C. Chu, H. Wu, J. Wang, J. Wang, Z. Li, J. Guo, G. Xu, Rheological behavior of titania ink and mechanical properties of titania ceramic structures by 3D direct ink writing using high solid loading titania ceramic ink, J. Alloys Compd. 783 (2019) 321–328, https://doi.org/10.1016/j.jallcom.2018.12.334.
[55] H. Du, C. Courrégelongue, J. Xto, A. Böhlen, M. Steinacher, C.N. Borca, T. Huthwelker, E. Amstad, Additives: their influence on the humidity- and pressure-induced crystallization of amorphous CaCO 3, Chem. Mater. 32 (2020) 4282–4291, https://doi.org/10.1021/acs.chemmater.0c00975.
[56] T.Y.-J. Han, J. Aizenberg, Calcium carbonate storage in amorphous form and its template-induced crystallization †, Chem. Mater. 20 (2008) 1064–1068, https://doi.org/10.1021/cm702032v.
[57] S. Raz, O. Testeniere, A. Hecker, S. Weiner, G. Luquet, Stable Amorphous calcium carbonate is the main component of the calcium storage structures of the Crustacean orchestia cavimana, Biol. Bull. 203 (2002) 269–274, https://doi.org/10.2307/1543569.
[58] J. Ihli, A.N. Kulak, F.C. Meldrum, Freeze-drying yields stable and pure amorphous calcium carbonate (ACC), Chem. Commun. 49 (2013) 3134, https://doi.org/10.1039/c3cc40807h.
[59] M. Farhadi Khouzani, D.M. Chevrier, P. Güttlein, K. Hauser, P. Zhang, N. Hedin, D. Gebauer, Disordered amorphous calcium carbonate from direct precipitation, CrystEngComm 17 (2015) 4842–4849, https://doi.org/10.1039/C5CE00720H.
[60] J.M. Xto, C.N. Borca, J.A. van Bokhoven, T. Huthwelker, Aerosol-based synthesis of pure and stable amorphous calcium carbonate, Chem. Commun. 55 (2019) 10725–10728, https://doi.org/10.1039/C9CC03749G.
[61] J. Jiang, M.-R. Gao, Y.-H. Qiu, S.-H. Yu, Gram-scale, low-cost, rapid synthesis of highly stable Mg–ACC nanoparticles and their long-term preservation, Nanoscale 2 (2010) 2358, https://doi.org/10.1039/c0nr00443j.
[62] H.K. Alber, Hygroscopic substances in microanalysis, Mikrochemie 25 (1938) 167–181, https://doi.org/10.1007/BF02714760.
[63] N. Bianco-Stein, I. Polishchuk, G. Seiden, J. Villanova, A. Rack, P. Zaslansky, B. Pokroy, Helical microstructures of the mineralized coralline red algae determine their mechanical properties, Adv. Sci. 7 (2020) 2000108, https://doi.org/10.1002/advs.202000108.
[64] B. Pokroy, A. Fitch, E. Zolotoyabko, The microstructure of biogenic calcite: a view by high-resolution synchrotron powder diffraction, Adv. Mater. 18 (2006) 2363–2368, https://doi.org/10.1002/adma.200600714.